THE ASTROPHYSICAL JOURNAL, 431:74–90, 1994 August 10

ARC STATISTICS AND CONSTRAINTS ON CLUSTER LENSES

SCOTT A. GROSSMAN AND PRASENJIT SAHA
Canadian Institute for Theoretical Astrophysics, McLennan Labs, University of Toronto,
60 St. George Street, Toronto, Ontario, Canada, M5S 1A7
Received 1993 August 11; accepted 1994 February 10

ABSTRACT

We investigate the statistical distributions of lengths and widths of gravitational arcs found in cluster lenses. Two lens models are considered: the nonsingular isothermal sphere (NSIS) and a new model we call "quasi–de Vaucouleurs" (QDEV), whose surface density resembles the de Vaucouleurs profile but is simpler for analytic study. Lensing cross sections are derived and convolved with a power-law distribution of source sizes. We apply selection criteria on the length-to-width ratio and on the length of arcs to our computation, since only arcs with $L/W \gtrsim 3$ and $L \gtrsim 2''.0$ should enter observational data sets. Comparing the model predictions with data on 85 arcs, we constrain the scaled core radii, r_c/b, of the lenses, where b measures the lens scale. In the NSIS lens, scaled core radii must be $r_c/b \lesssim 0.1$. In the QDEV lens, the scaled core radius has both upper and lower limits, $0.5 < r_c/b < 0.6$, excluding the point lens. These limits are only moderately sensitive to the slope of the distribution of source sizes. The strongest constraints come from the width analysis, where we fit the observed fraction of arcs (5%) with widths $W \geq 1''.3$. We derive a formula for the radii of curvature of arcs in any lens with a quadrupole perturbation. Analysis of the observed radii of curvature of giant arcs favors cluster profiles that are steeper than isothermal. We find that future observations of arc widths and of the unlensed sizes of faint field galaxies will be most useful for constraining the radial profile of cluster lenses.

Subject headings: galaxies: clustering — gravitational lensing

1. INTRODUCTION

Gravitational imaging of high redshift galaxies that have been lensed by foreground galaxy clusters has been an area of vigorous investigation since the discovery of the giant arcs in A370 and Cl2244 (Lynds & Petrosian 1986; Soucail et al. 1987a). In a mere 7 years after these early discoveries, there are now more than 20 clusters which have at least one candidate arc (see Fort 1992 for a recent review), and over half of these cases already can be regarded as secure lenses (Blandford & Narayan 1992).

The arcs provide a probe of the cluster's gravitational potential and allow the study of how mass traces light in galaxy clusters. Giant arcs form near critical lines of lenses, permitting a fairly robust estimate of the amount of mass enclosed within the arc if its redshift is known. Many detailed models of giant arcs have been constructed (see Blandford & Narayan 1992 for a list of references and general implications), and most have required lenses with smaller core radii (< 100 kpc) than is indicated by optical or X-ray images of the clusters. In some cases, the light does not trace the dark matter, and in some the dark matter must be significantly elliptical. For example, all these effects (small core radius and elliptial dark matter which is not traced by the light) are exhibited by models of the giant arc in A370 (Grossman & Narayan 1989; Hammer & Rigaut 1989; Bergmann, Petrosian, & Lynds 1990; Knieb et al. 1993).

Although the giant arcs constrain the mass in the core of a cluster very well, they provide only limited information about the mass profile of the cluster. Their widths are related to the local gradient of the mass profile (Hammer 1991), but information about the mass profile at other radii can only come from observations of weaker lensing. These weak lensing events do not trace the lens geometry as well, but they are predicted to be much more common (Grossman & Narayan 1988; Nemiroff & Dekel 1989). Thus, they can be used to trace the lens mass statistically.

Arclets (the weak lensing analog of giant arcs) were first seen in the cluster A370 (Fort et al. 1988), and soon after Tyson et al. (1990) found enough arclets (up to 60) in a single cluster to investigate in detail its mass profile. Observations such as these have prompted theoretical studies of the statistics of arcs under various assumptions about the lenses, sources, and cosmological parameters. For example, the number of giant arcs expected over the entire sky was calculated by Wu & Hammer (1993) for galaxy clusters that are described by nonsingular isothermal, modified Hubble and de Vaucouleurs ($r^{1/4}$ law) profiles. They find that arcs with length-to-width ratios $L/W > 10$ should be present in about half of rich clusters if they have $r^{1/4}$ law profiles, but should be less common, maybe by more than a factor of 10, if clusters have nonsingular isothermal profiles. Miralda-Escudé (1993a, b) studied in detail the statistics of arc lengths, widths, and radii of curvature for nonsingular isothermal models with quadrupole perturbation. He also considered the case of bimodal potentials. Bergmann & Petrosian (1993) focus on the statistical length and magnification distributions for elliptical lenses of finite mass. They show how the effect of finite source size and an elliptical lens combine to enhance the number of giant arcs over the number predicted for a spherical lens with point sources.

There have been only a few attempts to use observations to constrain cluster mass profiles, beginning with construction by Tyson et al. (1990) of a cluster "distortion profile." Kaiser & Squires (1993; see also Miralda-Escudé 1991 and Kochanek 1990) developed a mass inversion technique and applied it to the numerous arcs in A1689. In addition, Hammer (1991) inferred that clusters may be steeper than isothermal because arcs are thinner than the diameters of galaxies in faint-field galaxy surveys (Lilly, Cowie, & Gardner 1991; Tyson 1988). This conclusion is based on the questionable assumption that most faint field galaxies are marginally resolved

(i.e., $\gtrsim 1''.0$ in diameter). In general, however, statistical lensing has been exploited rather little so far to constrain the mass profile of galaxy clusters.

In this work we try to constrain models of galaxy cluster profiles using all the available data on arcs. We compare the data against two lensing models which we are unable to study analytically. The first model is the nonsingular isothermal sphere, which was treated numerically previously (Wu & Hammer 1993; Miralda-Escudé 1993a, b). The density profile is less steep than (but approaching) an isothermal profile outside the core. The second model was designed to resemble an $r^{1/4}$ law potential for an appropriate choice of core radius. In this case the profile is steeper than isothermal outside the core. The detailed numerical calculations of the number of arcs and their distribution of lengths and widths (Wu & Hammer 1993; Miralda-Escudé 1993a, b; Bergmann & Petrosian 1993) make predictions that our analytic treatment does not (e.g., the effects of partial caustic coverage by sources of finite size). However, the length and width distributions are much more sensitive to other uncertainties, such as the size distribution of the sources, and comparing the data with more precise numerical treatments probably is not warranted yet. Thus, we derive results from analytic calculations whenever possible, to better emphasize results that are generic to lens models.

The outline of the paper is as follows. In § 2 we discuss the two families of lens models used in our study of arc statistics. In § 3 we derive the cross sections for length and width magnification. We discuss the multiple imaging properties of an ideal circular lens. The observations of arc lengths and widths are summarized in § 4. In § 5 we convolve the magnification cross sections with a reasonable model for the source galaxy sizes to predict the statistical distribution of arc lengths and widths. By comparing these distributions with the observations, we constrain the core radii of the cluster models and the sizes of the source galaxies. We also take the average number of arcs per cluster as a weak constraint on the lens parameters. In § 6 we consider how quadrupole perturbations to the lens models affect the radius of curvature of arcs and compare observed curvatures of giant arcs with predictions. We summarize the results in § 7.

2. THE LENS MODELS

A wide range of lens models for galaxies and clusters of galaxies have been investigated numerically, but analytic studies have been confined mainly to the singular isothermal sphere (SIS) (e.g., Turner, Ostriker, & Gott 1984) and to nonsingular (e.g., Hinshaw & Krauss 1987) and noncircular (e.g., Kovner 1987) generalizations of the SIS. In this section, we introduce a lens model that resembles elliptical galaxy models such as de Vaucouleurs. It has finite mass and is more compact than the SIS. We will refer to it as the quasi–de Vaucouleurs (QDEV) model. Later in this paper we will compare the statistical properties of arcs produced by this model with those produced by the nonsingular isothermal sphere (NSIS), which is less compact than the SIS.

The QDEV and NSIS models are meant to represent two extremes whose properties are sufficiently different from each other than the data can select between them. In principle we could write one model profile whose steepness is parameterized so that it can be as shallow as an NSIS lens or as compact as a QDEV lens (e.g., Blandford & Kochanek 1987). However, we prefer to avoid adding an additional parameter which, we expect, can be constrained only broadly.

2.1. *The Quasi–de Vaucouleurs (QDEV) Model*

The quasi–de Vaucouleurs model (QDEV) is defined by the gravitational deflection

$$\alpha(r) = \alpha_0 r_c \frac{r}{(r_c + r)^2}, \tag{1}$$

where

$$\alpha_0 = \frac{4GM}{D_{\rm OL} r_c c^2}. \tag{2}$$

The total mass of the lens is M, and the core radius is r_c. The radial distance r is measured in terms of the angle subtended on the sky, so that the actual linear distance in the lens plane is $D_{\rm OL} r$, where $D_{\rm OL}$ is the angular diameter distance between observer and lens. This bending law is plotted in Figure 1. A similar deflection law, possessing a core radius and the same asymptotic behavior at large r, has been investigated by Bergmann & Petrosian (1993).

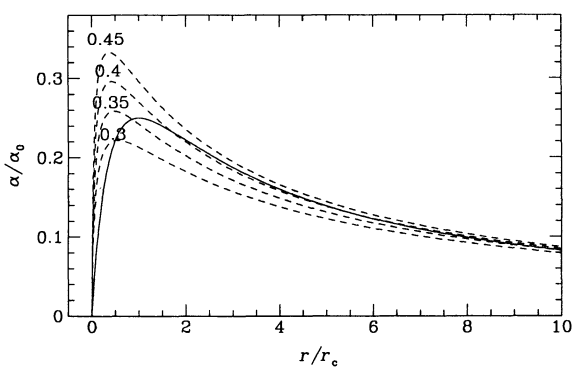

FIG. 1.—The *solid curve* shows the bending law for the QDEV lens, and the *dashed curves* show the de Vaucouleurs bending law for a lens with the indicated values of r_c/r_e. Asymptotically, all the curves are the same, but overall agreement is best for $r_c/r_e = 0.35$–0.4.

For comparison, the de Vaucouleurs bending law (Sanitt 1976), derived under the assumption of constant mass-to-light ratio in a lense with a de Vaucouleurs light profile, also is shown in Figure 1 for several values of the effective radius r_e, which encloses half of the mass. All these curves are asymptotically equivalent at large r since the models have finite mass. These de Vaucouleurs deflection curves are parameterized by the ratio r_c/r_e, and the best agreement between with the QDEV curve is obtained for $r_c/r_e = 0.35$–0.4. (Note that the application of the QDEV model to cluster lensing need not be justified by its similarity to the de Vaucouleurs model, but the QDEV model also may be useful in the investigation of galaxy lensing, and hence we compare the two models.)

The main advantage of the QDEV bending law is that its lensing properties are much simpler to calculate. An additional advantage is that its two-dimensional potential is known analytically and is given by

$$\phi(r) = 2GM\left[\ln\left(\frac{r_c + r}{r_c}\right) - \frac{r}{r_c + r}\right]. \tag{3}$$

The corresponding surface density is given by

$$\Sigma(r) = \frac{M}{D_{\rm OL}^2 \pi}\frac{r_c}{(r_c + r)^3}. \tag{4}$$

For this density profile with $r_c = 0.4r_e$, the amount of mass enclosed within radius $r \gtrsim 1.2r_c$ differs from the actual de Vaucouleurs computation by less than 3%. This model, however, lacks the central density cusp of the de Vaucouleurs profile, and within $r \lesssim 0.25r_c$ the differences exceed factors of 2.

From an Abel inversion of the surface density (e.g., Binney & Tremaine 1987), we obtain the three-dimensional density of the QDEV model,

$$\rho(R) = \begin{cases} \dfrac{3M}{2\pi D_{\rm OL}^3} r_c \left\{\dfrac{11r_c^2 + 4R^2}{3(R^2 - r_c^2)^3} - \dfrac{r_c(2r_c^2 + 3R^2)}{(r_c^2 - R^2)^{7/2}} \ln\left[\dfrac{r_c - (r_c^2 - R^2)^{1/2}}{R}\right]\right\}, & R \le r_c, \\ \dfrac{3M}{2\pi D_{\rm OL}^3} r_c \left\{\dfrac{11r_c^2 + 4R^2}{3(R^2 - r_c^2)^3} - \dfrac{r_c(2r_c^2 + 3R^2)}{(R^2 - r_c^2)^{7/2}} \tan^{-1}\left[\dfrac{(R^2 - r_c^2)^{1/2}}{r_c}\right]\right\}, & R \ge r_c, \end{cases} \tag{5}$$

where R is the three-dimensional radius measured in the same angular units as r or r_c. An expansion around r_c shows that this profile is both continuous and analytic at $R = r_c$, where $\rho(r_c) = (6/35\pi)(M/D_{\rm OL}^3 r_c^3)$.

The QDEV model shares with several alternative models for ellipticals (Binney 1982; Jaffe 1983; Hernquist 1990) the property that the surface density falls as r^{-3} at large r. These other models have simple three-dimensional densities, since they were designed for applications to dynamics, while the QDEV model differs by having a simple two-dimensional density, but a complicated three-dimensional density. The Binney and Jaffe models are known to reproduce elliptical galaxy profiles as well or better than the de Vaucouleurs model, and Dubinski & Carlberg (1991) showed that CDM halos are fitted well by the Hernquist profile, with a mean core radius of ~ 25 kpc (corresponding to $10'' h_{100}$ at $z_L = 0.3$). By implication, the QDEV mode may represent more accurately the properties of ellipticals than the $r^{1/4}$ law (except in the most central region). Thus, although the $r^{1/4}$ law has been used to model galaxy lenses in multiple quasar studies (Sanitt 1976; Dyer 1984; Maoz & Rix 1993) and galaxies within cluster lenses (Hammer & Rigaut 1989), such computations may not represent best the true nature of the lens. Certainly there is no reason to use an $r^{1/4}$ law cluster profile (Wu & Hammer 1993) other than its familiarity, since simpler models are as plausible.

2.2. *Nonsingular Isothermal Sphere (NSIS)*

Our second family of lens models, the NSIS lens, has been discussed in detail by several authors (e.g., Wu 1989; Hinshaw & Krauss 1987). Here we define the main physical properties of this model.

The surface density is given by

$$\Sigma(r) = \frac{\sigma_{\rm los}^2}{2GD_{\rm OL}}(r_c^2 + r^2)^{-1/2}, \tag{6}$$

where $\sigma_{\rm los}$ is the line-of-sight velocity dispersion and r_c is the core radius. Integrating the total mass inside radius r, we obtain the bending law,

$$\alpha(r) = \frac{4\pi\sigma_{\rm los}^2}{c^2}\left[\frac{\sqrt{r_c^2 + r^2} - r_c}{r}\right]. \tag{7}$$

Equation (7) too can be integrated to give the two-dimensional potential,

$$\phi(r) = 2\pi\sigma_{\rm los}^2 D_{\rm OL}[\sqrt{r_c^2 + r^2} + r_c \ln(\sqrt{r_c^2 + r^2} - r_c)]. \tag{8}$$

3. LENGTH AND WIDTH CROSS SECTIONS

In this section we compute cross sections for obtaining images with a particular tangential (length) magnification M_T, or radial (width) magnification M_R. The two components of magnification are given by eigenvalues of the magnification matrix, and if the lens is circular, they are

$$M_T^{-1} = 1 - \frac{D_{\rm LS}}{D_{\rm OS}}\frac{\alpha}{r}, \tag{9a}$$

$$M_R^{-1} = 1 - \frac{D_{\rm LS}}{D_{\rm OS}}\frac{d\alpha}{dr}, \tag{9b}$$

where the ratio D_{LS}/D_{OS} is the ratio of lens-source to observer-source angular diameter distances. Although it is customary to define magnifications as the absolute values of the eigenvalues, we admit the possibility of negative values. A "negative magnification" indicates a parity reversal of the source configuration.

Inverting equations (9a) or (9b) to find $r(M_R)$ or $r(M_T)$ and substituting into the lens equation gives the source position $r_s(M_R)$ or $r_s(M_T)$ corresponding to an image of radial magnification M_R or tangential magnification M_T. The lensing cross section σ to get images of a particular property is simply πr_s^2. In general, the inversion of equations (9) must be done numerically. However, we show below that for both the QDEV and NSIS models, σ can be computed analytically as a function of M_T. The cross section σ as a function of total magnification $M = M_R M_T$ can be computed only numerically (Wu 1993). While the cross section as a function of M is relevant for unresolved objects such as lensed quasars, its dependence on M_T and M_R individually are most interesting for resolved objects like luminous arcs.

The cross sections are proportional to an overall scale πb^2, where b turns out to be the Einstein radius of the singular lens models. For the QDEV model, b is defined by

$$b^2 = r_c \alpha_0 \frac{D_{LS}}{D_{OS}}, \tag{10}$$

where α_0 is given by equation (2). The scale for the NSIS model is set by

$$b = \frac{4\pi\sigma_{los}^2}{c^2} \frac{D_{LS}}{D_{OS}}. \tag{11}$$

3.1. *Tangential Magnification*

For the QDEV model the tangential magnification as a function of image position is given by

$$M_T^{-1} = 1 - \frac{b^2}{(r_c + r)^2}. \tag{12}$$

This relation, quadratic in r, can be inverted to yield

$$r = \left(\frac{b^2 M_T}{M_T - 1}\right)^{1/2} - r_c. \tag{13}$$

The tangential magnification is infinite at $r = b - r_c$, which defines the radius of the tangential critical line or Einstein ring. Lenses with $r_c > b$ are subcritical and incapable of multiple imaging. The tangential magnification cross section is

$$\sigma = \pi b^2 \left\{\left[\frac{1}{M_T(M_T - 1)}\right]^{1/2} - \frac{r_c}{bM_T}\right\}^2. \tag{14}$$

For the NSIS lens, the tangential magnification cross section is

$$\sigma = \pi b^2 \left[\frac{1}{(M_T - 1)^2} - \frac{2r_c}{bM_T(M_T - 1)}\right]. \tag{15}$$

Supercritical models have $r_c < b/2$. At large M_T, $\sigma \sim M_T^{-2}$ for both the QDEV and NSIS lenses, which is generic for fold caustics (e.g., Blandford & Narayan 1986). However, all supercritical NSIS lenses have a steeper cross section than QDEV lenses (see Fig. 2 below), leading to more weak magnification events in this case. Marginal and subcritical lenses do not share the same asymptotic properties, and in fact, the cross sections go to zero at a finite magnification M_T.

The tangential cross sections for the QDEV and NSIS models at both positive and negative M_T are plotted in Figure 2 for a range of core radii. Figure 2 illustrates well-known, generic properties of circular lenses (e.g., Blandford & Kochanek 1987). We review the lens behavior here since our discussion in terms of cross sections is somewhat novel. The source position r_s defines a cross section $\sigma = \pi r_s^2$, and if one draws a horizontal line at constant σ, the point at which it intersects the curve gives the tangential magnification M_T for the image. When a source is far from the center of the lens, gravitational lensing produces only one image with positive M_T. As the source moves closer to the lens center and the cross section decreases, M_T increases, and eventually a horizontal line at constant σ also intersects a curve at negative M_T. The points of these two additional intersections give the tangential magnifications of two new images that appear and separate across the radial critical line. As the source moves yet closer to the center of the lens, one of the new image moves toward the center of the lens with decreasing M_T and one moves outward, with M_T approaching negative infinity. At the same time, M_T of the principal image is approaching positive infinity, and the two bright images form an arc/counterarc pair. When the source is on the optical axis and the cross section goes to zero, the two bright images merge at the tangential critical line to form an Einstein ring. Figure 2 also shows that the cross section for generating multiple images is formally infinite for a point mass ($r_c = 0$), but for larger core radii, this cross section is finite and goes to zero when $r_c = b$.

Most cluster lenses with giant arcs do not show a long counterarc because they are not circular in general. Their gravitational potentials often have a quadrupole perturbation, and in this case, the point caustic at the center of the lens unfolds into an astroid, leading to the existence of a finite cross section for five images. The radial caustic can also undergo qualitative changes and may even be absent altogether (e.g., Wallington & Narayan 1993). Clearly, then, the cross section for strong lensing events and for multiple imaging can be strongly modified in noncircular lenses. The detailed behavior of the cross sections for multiple imaging are not robust for realistic cluster lenses, but the cross section for the principal image described by the curves at positive M_T is more robust, especially for weaker magnifications where the source is farther from a caustic.

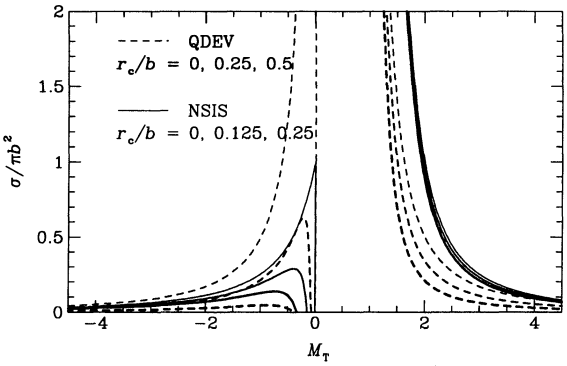

FIG. 2

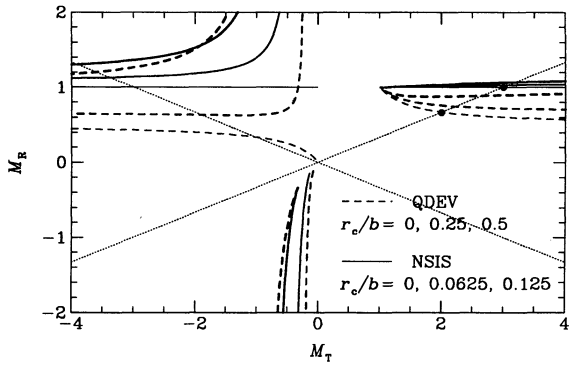

FIG. 3

FIG. 2.—The cross section to obtain images of tangential magnification M_T. Curves for several values of the core radius for both the QDEV and NSIS models are shown. The thinnest curves are for the smallest core radii. Images are located where a line of constant σ crosses the curves. There is always one image at positive M_T, the principal image, and it lies outside the tangential critical line. If there is an additional pair of images, one is demagnified in the core and one is a counter arc.

FIG. 3.—Radial magnification versus tangential magnification for several values of the core radius for both the QDEV and NSIS models. The thinnest curves are for the smallest core radii. The principal image is described by the curves at positive M_T. At the radial critical line, which corresponds to a particular negative value of M_T, two new images appear with opposite parity, $M_R = \pm\infty$. The dotted lines are defined by $M_T/M_R = \pm 3$, and images that lie between these lines would probably be detected as arcs. This degree of distortion is reached at $M_T = 2$ for a point lens and at $M_T = 3$ for a SIS, as indicated by the dots.

3.2. *Radial Magnification*

The radial magnification of an SIS lens is precisely unity, while arcs formed by steeper lenses are thinner and ones formed by shallower lenses are thicker (Miralda-Escudé 1993a; Hammer 1991). For the NSIS and QDEV lenses M_R is cubic in r. In principle, the cubic can be inverted and cross sections computed directly, but in a more simple analysis we substitute the relation between r and M_T (eq. [13] for the QDEV model) into equation (9b) and parameterize M_R by M_T. Then we will know both σ and M_R, parameterized by M_T.

For the QDEV model, the radial magnification is given by

$$M_R^{-1} = 2 - \frac{1}{M_T} - 2\frac{a}{b}\left(1 - \frac{1}{M_T}\right)^{3/2} . \tag{16}$$

The radial magnification for the NSIS lens is given by

$$M_R^{-1} = 1 - \left(1 - \frac{1}{M_T}\right)\frac{r_c/b}{M_T/(M_T - 1) - r_c/b} . \tag{17}$$

These results are plotted in Figure 3, which we now explain. A source far from the center of the lens must be only weakly distorted, so $M_T \approx M_R \approx 1$, corresponding to the point at positive M_T where the curves converge. As the source moves closer to the lens center and M_T increases, its image becomes thinner (thicker) for the QDEV (NSIS) model, as shown by the dashed (solid) curves at positive M_T, and asymptotically approaches its smallest (largest) value at the Einstein radius where $M_T \to \infty$. Smaller core radii favor smaller M_R. Eventually when the source crosses the radial caustic, two new images, with infinite radial magnification and opposite parity, appear at the value of M_T where the cross section of Figure 2 has a maximum. That is, one of the new images enters this figure from the top and one from the bottom at negative M_T. As the source moves farther toward the center, one image moves into the core with decreasing M_R and M_T, while the other image moves toward the tangential critical line, with M_R that asymptotically approaches the minimum value. Thus, when the arc/counterarc pair merges on the Einstein ring, the curves connect from the left ($M_T = -\infty$) to the curves at the right ($M_T = +\infty$).

Figure 3 also shows that for larger core radii the additional pair of images forms on the radial critical line with larger $|M_T|$ (i.e., farther leftward in Fig. 3). Thus, in lenses that are barely supercritical, images with large M_R also must have large M_T. The reason is that the radial and tangential critical lines are both approaching the center of the lens and getting closer to each other. The lens is approaching the hyperbolic-umbilic catastrophe (e.g., Miralda-Escudé 1993a), which, strictly speaking, is obtained only for a marginally supercritical lens.

In Figure 4 we plot the cross sections for radial magnification, where both σ and M_R have been parameterized by M_T. This figure can be interpreted in much the same way as Figure 2 for the tangential magnification. For a source at some radius and corresponding cross section σ, the radial magnifications of the images can be found by drawing a line across the figure at constant σ. At large σ where the source is far from the lens, only one image appears (except for the point lens). As the source moves closer to the lens, whether M_R increases or decreases depends on the particular lens model. For lenses with nonzero core radii, two additional images eventually appear as the source gets closer to the lens. One enters this figure from the left and one from the right with opposite parity and infinite magnifications. As the source moves closer toward the center of the lens, the image corresponding to the curve on the left moves toward the center and gets demagnified by the core, while the other image, the counter arc, moves toward the critical line to ultimately merge with the principle image where the cross section is zero. If we consider the models plotted here as spanning a reasonable range for realistic clusters, we see that the minimum width of an Einstein ring is $M_R = \frac{1}{2}$ (for the point lens) and may be a few times bigger for an NSIS lens with significant core radius. Thus, the variation of arc widths can be a powerful constraint on lens models (Hammer 1991), a fact we shall exploit later.

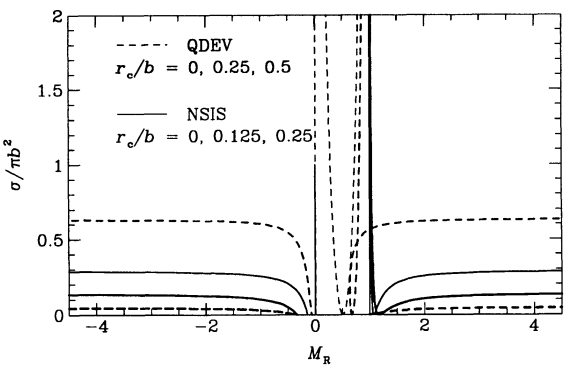

FIG. 4.—The cross section to obtain images of radial magnification M_R. A range of core radii for both the QDEV and NSIS models are shown. Images are located where a line of constant σ crosses the curves. When two images appear across the radial critical line, one image is demagnified in the core and the other merges with the principle image at the M_R of the Einstein ring.

As before, we caution that these cross sections for multiple images are valid only for very circular potentials, and, in general, the cross sections for multiple images are not very robust. The cross sections for the principal image are more robust, however, since that branch of solutions includes weak lensing for sources farther from the caustics.

4. OBSERVATIONS

Since the initial identification of giant arcs in the galaxy clusters A370 (Soucail et al. 1987a; Lynds & Petrosian 1986) and 2244−02 (Lynds & Petrosian 1986), several more giant arcs have been found. In addition, surveys for smaller arclets have also proved successful (Pello et al. 1992; Smail et al. 1991), increasing the number of arc candidates considerably. In Table 1 we have compiled a list of arc candidates that we regard as likely lensed images of distant galaxies. There are 96 entries representing 20 cluster lenses. Only arcs which have been specifically identified in the literature, either by assignment of a name or by having some property (magnitidue or dimensions) measured, are included. Thus, many of the faint distorted images seen by some authors (Tyson, Valdes, & Wenk 1990; Fort 1992) have not been included since no quantitative information is available on individual objects. Table 1 is probably nearly complete as of the writing of this paper.

There are 85 objects in Table 1 with measured lengths, 10 of which have $L > 10''.0$. Among these 85 arc candidates, only 10 have measured widths and only eight have measured redshifts. Although a lensing interpretation is very likely for all the giant arcs, even for those without secure redshifts, one must bear in mind that the case is much less strong for the more common weak magnification candidates if their redshifts are unknown. No doubt there are some arc candidates in Table 1 that, in fact, are not lensed by the clusters, but judging by the photometric redshifts obtained by Pello et al. (1992), the contamination should be less than 25%. A few objects in the list have neither measured lengths, widths, nor redshifts, but do have measured magnitudes, and are included for completeness.

The arc candidates are typically, but not always, bluer in $B-R$ than the foreground cluster galaxies (e.g., Pello et al. 1992), but the primary criterion for any object to make this list is simply image morphology. An image whose ratio of length to width is sufficiently extreme is a good arc candidate. Smail et al. (1991) take as arc candidates images with $L/W > 2$, and Pello et al. (1992) use $L/W > 3$. Thus, in surveys made under reasonable seeing conditions, say $0''.7$ to $1''.2$, only images with $L \gtrsim 2''.0$ should enter the candidate list. In the following section we adopt the practical limits of $L/W > 3$ and $L > 2''.0$ as the criteria for arc detection.

5. ARC STATISTICS AND OBSERVATIONAL CONSTRAINTS

If all sources have the same unlensed angular diameter L_0, then the distributions of lengths and widths are described simply by the cross sections given in § 3, where lengths are scaled by $L = L_0 M_T$ and widths by $W = L_0 M_R$. In a more general calculation of the length and width distributions, the cosmological distribution of source redshifts enters through the parameter b, and at each redshift, the sources have a distribution of angular sizes. Then, the distribution of arc lengths and widths must be derived by convolutions over the redshift and angular size distributions of the sources. These convolutions usually cannot be done analytically.

To simplify our calculations and to better emphasize the key physical ideas, we make some simplifying assumptions that still yield approximately correct quantitative results. We note that most arcs with measured redshifts have $z_s \approx 1$, and that the effect of moving them to higher redshift, say $z_s \approx 2$, is to increase their number by about a factor of 2. On the other hand, the number of arcs is much more sensitive to the unlensed angular size of the sources (Miralda-Escudé 1993b). As our first assumption, we take b as fixed, independent of cosmological parameters. (This is equivalent to placing all sources at a single redshift.) Similarly, we do not consider how the angular sizes of the sources may be correlated with redshift, but use a simple model, described below, as our second assumption. These simplifying cosmological assumptions are essentially the same as used by Miralda-Escudé (1993a, b), who takes all sources to be at a single redshift with sizes that do not depend directly on the redshifts.

We assume the distribution of angular source size L_0 has the form

$$\frac{d^2N}{d\Omega\, dL_0} = \frac{C}{L_0^{\alpha}}, \qquad L_0^{\min} < L_0 < L_0^{\max}, \tag{18}$$

where $d\Omega$ is a solid angle, α is the slope of the distribution, and C is a constant to be calibrated by the observed density of faint field

TABLE 1

OBSERVED ARCS AND ARCLETS

Cluster	I.D.	z_l	z_s	L	W	References
A2218	33	0.171	...	4.8	...	1, 2
A2218	43	0.171	...	2.5	...	
A2218	67	0.171	...	3.2	...	
A2218	71	0.171	...	3.8	...	
A2218	190	0.171	...	3.2	...	
A2218	231	0.171	...	2.6	...	
A2218	238	0.171	...	4.2	...	
A2218	254	0.171	...	4.9	...	
A2218	289	0.171	1.034	6.7	...	
A2218	300	0.171	...	2.2	...	
A2218	309	0.171	...	4.1	...	
A2218	323	0.171	...	4.0	...	
A2218	344	0.171	...	3.0	...	
A2218	359	0.171	0.702	5.8	...	
A2218	362	0.171	...	2.9	...	
A2218	365	0.171	...	3.4	...	
A2218	367	0.171	...	3.0	...	
A2218	382	0.171	...	5.1	...	
A2218	384	0.171	...	7.1	...	
A2218	431	0.171	...	5.0	...	
A2218	444	0.171	...	6.3	...	
A2218	456	0.171	...	4.3	...	
A2218	468	0.171	...	2.3	...	
A2218	476	0.171	...	2.5	...	
A2218	487	0.171	...	2.1	...	
A2218	508	0.171	...	2.7	...	
A2218	514	0.171	...	2.6	...	
A2218	537	0.171	...	4.9	...	
A2218	680	0.171	...	5.6	...	
A2218	684	0.171	...	2.6	...	
A2218	730	0.171	...	22.0	...	
A2218	731	0.171	...	3.3	...	
A2218	ring	0.171	...	25.8		
A963	...	0.206	...	22.6	<1	3, 4
A963	...	0.206	0.77	6.3	<1	
A222	A222-1	0.21	...	7.1	...	5
A222	A222-2	0.21	...	3.9	...	
A1942	A1942-1	0.22	...	4.5	...	5
A1942	A1942-2	0.22	...	3.0	...	
A1942	A1942-3	0.22	...	3.9	...	
AC 113	AC113-1	0.22	...	3.8	...	5
AC 113	AC113-2	0.22	...	3.8	...	
AC 113	AC113-3	0.22	...	3.9	...	
A2390	ABC	0.231	0.913	15	1.3	6
A2390	1	0.231	...	3.6	...	
A2390	2	0.231	...	3.6	...	
A2390	3	0.231	...	5.3	...	
A2390	4	0.231	...	4.6	...	
A2390	5	0.231	...	5.3	...	
A2390	6	0.231	...	4.7	...	
A2390	7	0.231	...	3.6	...	
A2390	D	0.231	0.913	3	...	
A2397	A2397-1	0.24	...	3.6	...	5
J2183−27T	J2183-1	0.28	...	3.3	...	5
AC 118	AC 118-1	0.31	...	4.4	...	5
AC 118	AC 118-2	0.31	...	5.4	...	
AC 118	AC 118-3	0.31	...	3.8	...	
AC 114	AC 114-1	0.31	...	3.5	...	5
AC 114	AC 114-2	0.31	...	6.9	...	
AC 114	AC 114-3	0.31	...	6.2	...	
MS 2137−23	A0	0.315	...	14.2	1.8	7
MS 2137−23	A1	0.315	...	3.5	0.9	
MS 2137−23	A2	0.315	...	...	...	
MS 2137−23	A3	0.315	...	...	...	
MS 2137−23	A4	0.315	...	...	...	
MS 2137−23	A5	0.315	...	...	...	
MS 2137−23	A6	0.315	...	...	...	

TABLE 1—*Continued*

Cluster	I.D.	z_l	z_s	L	W	References
MS 2137−23	A7	0.315	...	...	...	
MS 2137−23	A8	0.315	...	...	...	
MS 2137−23	A9	0.315	...	...	...	
MS 2137−23	A10	0.315	...	...	...	
0500−24	...	0.316	...	14	...	8, 9
2244−02	...	0.328	2.237	19	<0.5	10, 11, 12
0957+561	A_1	0.36	...	5.5	<1.2	13
0957+561	A_2	0.36	...	4.5	...	
A370	A0	0.373	0.724	21	0.8	10, 12, 14, 15, 16, 17, 18
A370	A1	0.373	...	3	<0.7	
A370	A2	0.373	...	4	...	
A370	A3	0.373	...	3	...	
A370	A4	0.373	...	2.5	...	
A370	A5	0.373	1.306	9.3	...	
A370	A6	0.373	...	7	...	
A370	B2	0.373	...	...	...	
A370	B3	0.373	...	...	...	
J2090−7CL	J2090-1	0.38	...	4.1	...	18
J2090−7CL	J2090-2	0.38	...	3.5	...	
0024+1654	A_1	0.39	>1	4	1	12, 19
0024+1654	B_1	0.39	>1	2	<0.7	
0024+1654	C_1	0.39	>1	4	1	
0024+1654	A_2	0.39	>1	6	1	
0024+1654	B_2	0.39	>1	4	<0.7	
0024+1654	C_2	0.39	>1	6	1	
0302+1658	A_1	0.423	...	10.7	1.4	20
0302+1658	A_2	0.423	...	7.8	1.4	
MS 1621.5+2640	...	0.426	...	9	<0.5	21
MS 2053.7−0449	...	0.583	...	11	<0.5	21

REFERENCES.—(1) Pello-Descayre et al. 1988; (2) Pello et al. 1992; (3) Lavery & Henry 1988; (4) Ellis, Allington-Smith, & Smail 1991; (5) Smail et al. 1991; (6) Pello et al. 1991; (7) Fort et al. 1992; (8) Giraud 1988; (9) Wambsganss et al. 1989; (10) Lynds & Petrosian 1989; (11) Hammer et al. 1989; (12) Mellier et al. 1991; (13) Bernstein, Tyson, & Kochanek 1992; (14) Soucail et al. 1987b; (15) Soucail et al. 1988; (16) Miller & Goodrich 1988; (17) Fort et al. 1988; (18) Kneib et al. 1993; (19) Kassiola, Kovner, & Fort 1992; (20) Mathez et al. 1992; (21) Luppino & Gioia 1992.

galaxies. (We note that if all galaxies are at a single redshift with a power-law luminosity function of slope -1 and if their luminosities are proportional to the square of their diameters, then $\alpha = 1$.) The figures we present in this section are for $\alpha = 1$, but we will discuss the consequences of varying α between 0.5 and 2.0. Since field galaxies to $V = 26.5$ have half light diameters up to $\sim 1''.5$ (Lilly, Cowie, & Gardner 1991) and few are larger, we take the maximum angular size to be $L_0^{\max} = 1''.5$. (The half light diameter corresponds to the FWHM of a Gaussian profile, which is the value usually reported for arc widths. Thus, when we compute arc widths, we do not have to worry about the detailed luminosity profile of the sources.) However, the seeing limit of Lilly et al.'s observations is not very much smaller, so that the distribution of L_0 or its lower limit $L_0^{\min}$ is not well-determined. Below we consider values of $L_0^{\min}$ as small as $0''.15$ since such small galaxies occasionally may be lensed to resolved dimensions, but there is no observational support for the shape of the size distribution, equation (18), at such small dimensions. We use the ratio $L_0^{\max}/L_0^{\min}$ as a parameter of the calculation. Larger values of this parameter indicate a greater abundance of small source galaxies. Following Miralda-Escudé (1993b), we calibrate the constant C using a source density of 24 arcmin^{-2} galaxies in the magnitude range $25 < B < 26$, which is a compromise between the numbers observed by Lilly et al. (1991) and Tyson (1988).

Implicit in these calculations is the assumption that the sources are perfectly circular. The intrinsic non-circularity of the sources is important for predictions of very weak lensing (Miralda-Escudé 1991; Kaiser & Squires 1993; Kochanek 1990), but since we concern ourselves only with images with $L/W > 3$, this should be of minor importance here. Source ellipticity would add some random scattering to the computed distributions.

In addition to the distribution of lengths and widths, we calculate how many arcs are produced by each lens model of scale b. By comparing the observed arc length and width distributions and the observed number of arcs with predictions, we will place constraints on the lens models. These constraints will apply to characteristic rich cluster lenses. They may not be representative of individual clusters or of those with too little mass to be important in lens surveys.

5.1. *Length Distribution*

For the special case that $\alpha = 1$, the convolution of source size distribution with the lensing cross sections can be computed analytically. The formulae for the resulting length distributions are given in Appendix A. The resulting length distribution for the QDEV model is plotted in Figure 5. Curves for three values of the ratio $L_0^{\max}/L_0^{\min} = 1$, 2, 10 are shown. A larger ratio (more small sources) means fewer arcs at each length. That is, curves essentially shift to the left. The curves terminate at left where the ratio L/W

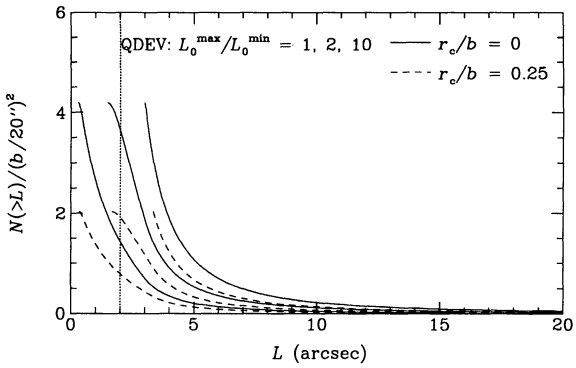

FIG. 5

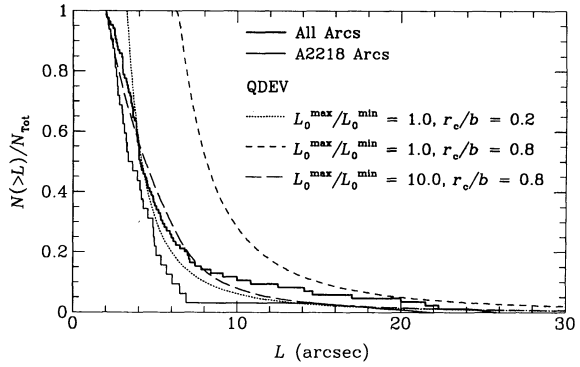

FIG. 6

FIG. 5.—The cumulative distribution of arc lengths for the QDEV model with core radii $r_c/b = 0$, 0.25. The parameter L_0^{max}/L_0^{min} takes on the values 1, 2, and 10, with curves farther to the left being dominated by smaller source galaxies. The curves terminate at the left where the ratio of L/W falls below 3. The lens scale is normalized to $b = 20''.0$, and there are 24 arcmin^{-2} sources. According to the detection criteria, arcs to the left of the dotted line at $L = 2''.0$ would not enter the data set.

FIG. 6.—The cumulative distribution of arc lengths for the complete sample of arcs in Table 1 is plotted as the heavy solid histogram, and the A2218 subsample is also shown for comparison. The predictions for a few parameter selections for the QDEV model are shown also, where we use $\alpha = 1$ for the slope of the angular size distribution of sources.

falls below 3. The number of arcs at each length depends strongly on the scaled core radius, with fewer arcs in lenses with larger values of this parameter. That is, curves essentially shift vertically. (However, larger core radii also produce wider arcs, so that the minimum L where $L/W = 3$ is also larger, causing a simultaneous shift to the right.)

The NSIS lens has a qualitatively similar length distribution, but it generally produces fewer arcs than the QDEV lens. To make a specific comparison, the singular NSIS model ($r_c/b = 0$) produces precisely half as many arcs as the singular QDEV lens (point lens) with the same b. This is because $L/W = 3$ when $M_T = 3$ in the first case and when $M_T = 2$ in the second, as shown by the dots in Figure 3. The corresponding ratio of cross sections (see eqs. [14] and [15]) is $\sigma_{QDEV}(M_T = 2)/\sigma_{NSIS}(M_T = 3) = 2$.

Finally, we address whether the distributions calculated here apply only to lenses with ideal circular symmetry, or whether they describe also more realistic lenses with quadrupole asymmetry. We previously pointed out that the distribution for weak lensing will be essentially unchanged by making the lens elliptical. However, the cross section for strong lensing may be significantly different, and the only way to get the distribution of arc properties is by numerical simulations. Miralda-Escudé (1993b) showed that the analytic SIS prediction breaks down for $L \gtrsim 15''$ if the ellipticity is $\epsilon = 0.2$ and $b = 20''.0$. Realistic distributions also have a cutoff at finite L, since no arc can have a length that exceeds the circumference of the Einstein ring. This obvious breakdown of the analytic prediction, resulting from a finite source size, manifests itself only at high magnifications. The numerical simulations of an elliptical lens with $\epsilon = 0.1$ by Bergmann & Petrosian (1993) showed that the distribution of arc opening angle (effectively arc length) follows the analytic prediction for a circular lens and finite source size up to an opening angle of $\sim 45°$ ($\sim 15''$ if $b = 20''.0$), beyond which there is an excess of giant arcs, followed in turn by a cutoff in the distribution. Thus, at intermediate or low magnifications, the analytic results presented here would be modified only slightly by lens ellipticity.

In principle, one could try to constrain the nature of the lenses by comparing the observed number of arcs with the predictions, but this comparison would depend upon the distribution of lensing scales b and the somewhat uncertain density of sources. Most of all, such a comparison would require better knowledge of the completeness of lens surveys than is known presently. Comparisons of the observed and predicted cumulative length distributions, normalized to unity, should lead to more robust constraints on lens models. Such a normalized distribution is independent of source density and lens scale b. (We will consider the predictions for the number of arcs later.)

In Figure 6 we show the normalized cumulative distribution of observed arcs for both the complete set of data in Table 1 and the A2218 subset. The two histograms are similar in the moderate magnification regime, but the rare high-magnification events are represented better in the full sample, which we prefer to use to set constraints. Indeed, giant arcs may be overrepresented in this complete sample, relative to model predictions. This may be partly an observational bias favoring the discovery of giant arcs instead of arclets, but Bergmann & Petrosian (1993) showed that more detailed models including the effects of finite source size and lens ellipticity can increase the numbers of giant arcs by factors of a few. Fortunately, since giant arcs still comprise a small fraction of the total, our simple models will suffice.

Predictions of the QDEV model are also shown in Figure 6 for three sets of parameters. The contours of the Kolmogorov-Smirnov (e.g., Press et al. 1986) probabilities over a grid of parameters are shown in Figure 7, where the parameters of the three models are shown in Figure 6. The dotted curve ($L_0^{max}/L_0^{min} = 1.0$, $r_c/b = 0.2$) appears to be in reasonable agreement with the data, but as the core radius is increased, the curves move to the right. The reason is that the arcs become thicker, so that the shortest arc meeting the $L/W > 3$ criterion is now longer. The short-dashed curve ($L_0^{max}/L_0^{min} = 1.0$, $r_c/b = 0.8$) shows a bad fit resulting from increasing the core radius too much. This curve, however, can be shifted back to the left by decreasing the source sizes (increasing L_0^{max}/L_0^{min}), thereby improving the quality of fit and explaining the gentle rise of the probability contours in Figure 7. If, however, L_0^{max}/L_0^{min} is sufficiently large, then the shortest arcs with $L/W > 3$ do not meet the detection criterion $L > 2''.0$. In this case we normalize distributions to the number of arcs predicted to have $L > 2''.0$ rather than the total number with $L/W > 3$. This is the case for the long-dashed curve ($L_0^{max}/L_0^{min} = 10.0$, $r_c/b = 0.8$) in Figure 6. For such large values of L_0^{max}/L_0^{min}, the agreement is hardly sensitive to the value of this parameter, and so the probability contours become almost vertical.

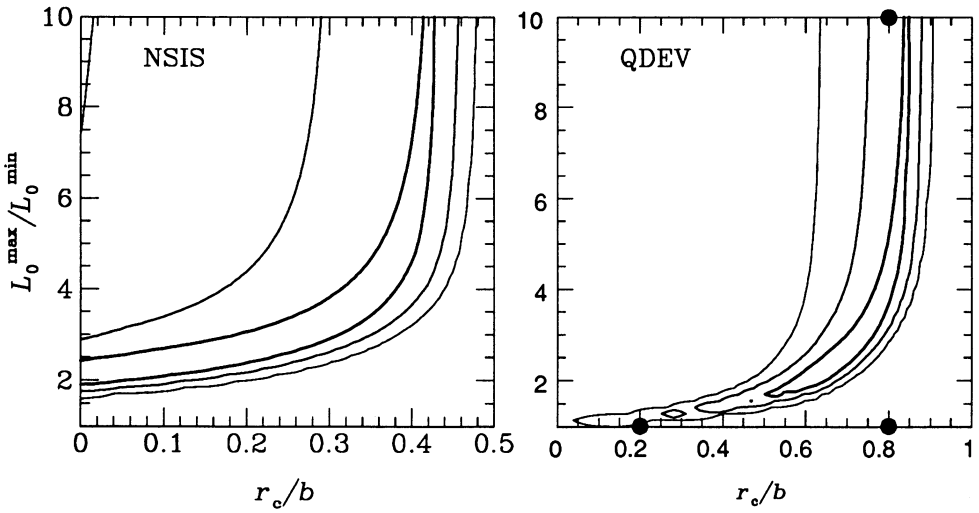

FIG. 7.—Contours of 1 σ, 2 σ, and 3 σ (*dark to light contours*) KS probability derived from a comparison of observed arc lengths to model predictions. The slope of the angular size distribution is $\alpha = 1$, and the contours are fairly insensitive to variations of this parameter. Most of parameter space remains allowed within 3 σ in the NSIS model (*left*), so constraints will have to come from other tests. In the QDEV panel (*right*), parameters of the three models shown in Fig. 6 are marked with dots.

We have explored the consequences of using different values of α, the slope of the unlensed angular size distribution, through a Monte Carlo computation where we select the source sizes L_0 and magnifications M_T from their probability distributions. Since we can calculate M_R from M_T, we get both the lengths and widths of arcs, to which we apply the selection criteria. Hence we find the length and width distribution of arcs. We find that $\alpha > 1$ moves the contours in Figure 7 only slightly to the right, and conversely for $\alpha < 1$.

We briefly discuss the effects we would expect if we allowed for intrinsically elliptical sources. The scatter of unlensed size L_0 due to the random orientation of an elliptical source would appear as a comparable scatter in magnified length L, where, say, each L could be scattered to smaller or larger lengths by factors of ~ 2. The main effect would be to make the steep part of the calculated distributions somewhat more shallow. We still expect, however, the best fits to be obtained with roughly the same parameters.

5.2. *Width Statistics*

In principle we can write an equation analogous to the results of Appendix A to describe the differential distribution dN/dW, but the integrals cannot be computed analytically since the cross sections are parameterized in terms of M_T and not M_R. Therefore, we use the Monte Carlo computation for all values of α. In addition, the $L > 2\farcs0$ detection criterion introduces a bias in the width distribution of arcs. In particular, we saw in Figure 5 that for some parameters there are arcs that do not meet the $L > 2\farcs0$ criterion. The arcs that are rejected by this criterion will usually have small sources, since a big length magnification is more improbable than a smaller one. The bias introduced into the source sizes of detected arcs will be reflected as a bias in the observed widths of arcs. That is, even if most sources are so small that their widths would be unresolved, arcs that meet the detection criteria will have a significantly larger fraction resolved. In extreme cases, the median arc width can be nearly 2 times larger than when the length criterion is not considered (Grossman 1994).

In principle, we could compare the observed width distribution to the predicted one, but the small fraction of arcs that have measured widths does not justify such a detailed comparison. Instead, we will compare the predicted number with $W \geq 1\farcs3$ to the observed number of 4, assuming Poisson uncertainty on the predicted number. (If this number is measured at smaller widths, the uncertain arises not only from the stochastic noise, but also from a systematic failure to resolve some arcs in inferior seeing. Unfortunately, using a large number closer to L_0^{max} makes this a less sensitive test.)

Probability contours are drawn in Figure 8. For the NSIS model, large core radii with $r_c/b \gtrsim 0.1$ produce too many arcs with $W \geq 1\farcs3$ and are excluded with 3 σ significance. A larger slope α for the unlensed angular size distribution of sources moves the contours to the right, and if $\alpha = 2$, then we exclude $r_c/b \gtrsim 0.3$ with 3 σ significance. In Figure 8, we see for the QDEV model that core radii with $r_c/b \gtrsim 0.6$ also produce too many wide arcs, but core radii $r_c/b \lesssim 0.5$ predict too few since $M_R < 1$ and even the largest sources would not satisfy the width criterion. Thus, point mass lenses are excluded. For values of α in the range 0.5–2.0, the lower limit on the contours stays at $r_c/b \gtrsim 0.5$, but if $\alpha = 2.0$, the upper limit moves to $r_c/b \lesssim 0.7$. Thus, the general conclusions of this section are fairly robust for a wide range of α. If most faint field galaxies are marginally resolved (i.e., L_0^{max}/L_0^{min} is within a factor of 2 of unity), then we confirm Hammer's (1991) result that the NSIS model is excluded in favor of lens models that are steeper than isothermal.

5.3. *Numbers of Arcs*

The number of arcs in a cluster depends on the source density and the cross section, which scales as b^2. The source density of 24 arcmin^{-2}, assumed in the computation for Figure 5, is probably reasonable for arc surveys that reach surface brightnesses of $\mu_V \approx 26.0$ arcsec^{-2} (Smail et al. 1991) or somewhat fainter in B ($\mu_B \approx 27$ arcsec^{-2}). The uncertainty is probably not more than a

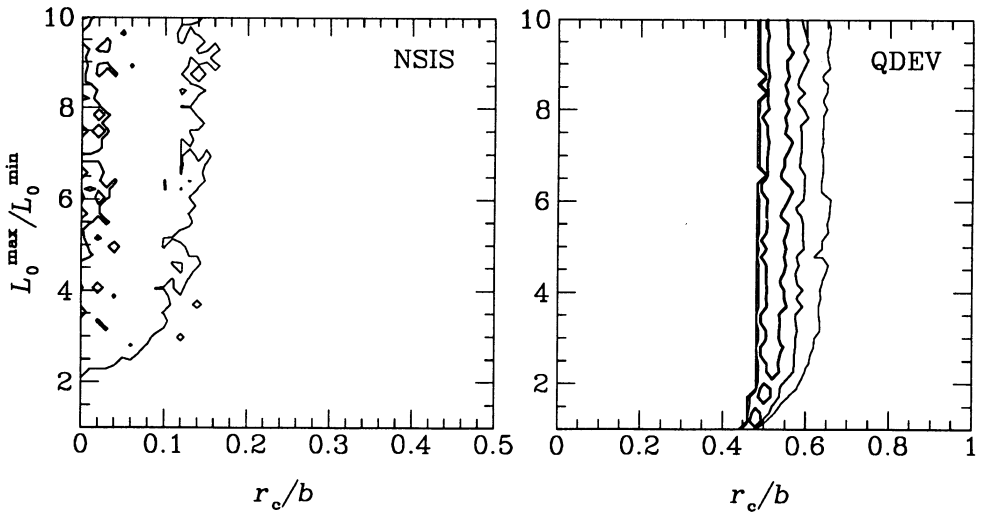

FIG. 8.—Contours of 1 σ, 2 σ, and 3 σ (*dark to light contours*) probability to get the observed fraction of arcs that have $W \geq 1''.3$. The slope of the angular size distribution is $\alpha = 1$, and larger values move the upper limits to the right. Models with large core radii produce too many resolved arcs, and in the QDEV lens, small core radii produce too few. The ripples in the contours result from noise in the Monte Carlo distribution of arc widths. *Left:* NSIS. *Right:* QDEV.

factor of 2. The choice of b, which depends upon lens redshift, source redshift, cosmological model, and lens mass, represents a much larger source of uncertainty. We consider each of these next.

The uncertainties arising from the choice of lens and source redshifts and cosmological model enter primarily through the ratio of angular diameter distances D_{LS}/D_{OS} (neglecting the possibility that these parameters may also be tied to source evolution). The mean redshift of clusters listed on Table 1 is $z_L = 0.31$, and the standard deviation is only ~ 0.1. The source redshifts are mostly unknown, but we consider as a plausible range $0.7 < z_s < 2.0$. Adopting the angular diameter distances for a homogeneous FRW cosmology with $\Omega = 1.0$ (e.g., Blandford & Narayan 1992), the ratio D_{LS}/D_{OS} varies between ~ 0.5 and 0.7.

Values of $b > 20''.0$ require velocity dispersions $\sigma_{los} \gtrsim 1200$ km s^{-1} or masses $M \gtrsim 2 \times 10^{15}\ M_\odot$. Although such values are extremely large for clusters (Girardi et al. 1993, Bahcall & Cen 1993), cluster lenses are often selected precisely because they are rich, are very X-ray luminous, or have a large σ_{los}. Therefore, we use $b = 20''.0$ as a characteristic value. In Figure 9 we draw contours in parameter space for producing 2, 1, 0.5, and 0.25 arcs per cluster (where arcs must meet the requirements $L/W > 3$ and $L > 2''.0$).

From the previous discussion it is apparent that there are several parameters, whose combined uncertainties make the prediction of arc numbers highly uncertain. More detailed information about source redshifts and lens masses would be required to make firmer predictions. (Note, however, that lens masses are usually inferred from lens calculations, rather than imaging properties derived from an assumed lens mass.) Thus, we do not use the predicted number of arcs to strongly constrain the model parameters. Nevertheless, models with nearly marginal core radii produce so few arcs, even for the most optimistic values of b, that such models should be rejected. Hence, we use the number of arcs per cluster as a weak constraint on the models, and assign probabilities to rule out only the weakest lenses.

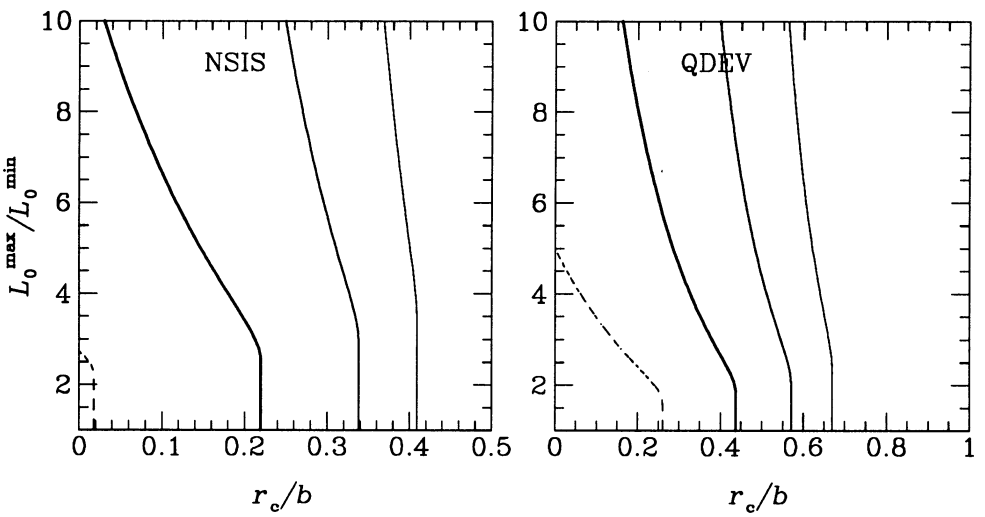

FIG. 9.—Contours of constant numbers of arcs per cluster, using 24 arcmin^{-2} source galaxies and $b = 20''.0$. This computation assumes a slope $\alpha = 1$ for the unlensed angular size distribution of sources. The dotted line is for 2 arcs per cluster, where an arc is any image with $L/W > 3$ and $L > 2''.0$. The solid contours (*dark to light*) are for 1, 0.5, and 0.25 arcs per cluster. These contours also represent the 1 σ, 2 σ, and 3 σ probability contours. *Left:* NSIS. *Right:* QDEV.

The largest number of arcs per cluster reported by any observer is 32 in A2218 (Pello et al. 1992). There are 96 arc candidates in Table 1 among 20 clusters, giving ~ 5 arcs per cluster. The survey of Smail et al. (1991) found 20 arc candidates in 19 clusters, giving ~ 1 arc per cluster. The intermediate value is probably a reasonable characteristic number for observations to $\mu_B \approx 27$ arcsec^{-2}.

Models that predict fewer than 1 arc per cluster would probably have no arcs and such clusters would not be represented in Table 1. We make a rather arbitrary probability assignment that these models should be rejected at the 1 σ level, and we consider that further decreases by factors of 2 (equivalent to reducing the velocity dispersion by a factor of 1.2 or the mass by 2) correspond to additional 1 σ decreases of probability. Thus the contours in Figure 9 for generating 1.0, 0.5, and 0.25 arcs per cluster are also the 1 σ, 2 σ, and 3 σ probability contours.

5.4. *Maximum-Likelihood Parameters*

We estimate the most likely model parameters by considering length, width, and number statistics in combination. For the NSIS model, the strongest constraints on parameter space come from the width data, and the length and number constraints are completely consistent. We conclude that if the NSIS model applies to clusters, then $r_c/b \lesssim 0.1$–0.3 for α in the range 0.5–2.0, and $L_0^{\max}/L_0^{\min} \gtrsim 2.0$.

For the QDEV model, the strongest constraints on parameter space also come from the width analysis, and most of the allowed parameter space is allowed also by the number analysis. We conclude that $0.5 \lesssim r_c/b \lesssim 0.6$–$0.7$ for α in the range 0.5–2.0. These constraints are consistent with the small core radii needed to model giant arcs.

If the smallest sources have diameters $L_0^{\min}$ much smaller than the observational resolution limit, they will contribute to the observed and theoretical length and width distributions only in the rare instances of high magnification. Thus, the statistical distributions are faily insensitive to the parameter $L_0^{\max}/L_0^{\min}$, and the constraints we can place on this parameter are weak.

6. RADIUS OF CURVATURE

In general, arcs in elliptical lenses do not form sections of circles, nor are they necessarily sections of the elliptical contours of constant density or potential. Their shapes depend on the detailed lens profile, permitting the possibility of using measurement of the radius of curvature R, not only as an indicator of the ellipticity of a lens, but also as a diagnostic of its radial profile. In this section we derive a formula for the radius of curvature for any lens model, and then we consider as particular cases elliptical generalizations of the QDEV and NSIS lens models. We will discuss the implications of the observed radii of curvature of arcs for cluster models.

The elliptical generalization of a circular lens with density profile $\Sigma_0(r)$ and deflection law $\alpha_0(r)$ (note that this function has a different meaning than the constant α_0 defined in eq. [2]) can be described by

$$\Sigma(r, \theta) = \Sigma_0[r(1 - \epsilon \cos 2\theta)^{1/2}] . \tag{19}$$

Assuming that terms of $O(\epsilon^2)$ are negligible, the potential can be written as a multipole expansion (Kochanek 1991; Schneider & Weiss 1991) to second order according to

$$\phi(r, \theta) = \phi_0(r) + \frac{\epsilon}{2} \phi_2(r) \cos 2\theta , \tag{20}$$

where,

$$\phi_0(r) = \frac{c^2 D_{OL}}{2} \int_0^r \alpha_0(r')dr' , \qquad \phi_2(r) = -\frac{4\pi G}{r^2} \int_0^r r'^3 \Sigma_0(r')dr' . \tag{21}$$

Substituting equation (20) for ϕ into equation (B14) for the radius of curvature (see Appendix B for a derivation), we obtain

$$\left(\frac{R}{r}\right)^{-1} = 1 - 2\epsilon \frac{(\partial/\partial r)[(1/r)\phi_2]}{r(\partial/\partial r)[(1/r)(\partial\phi_0/\partial r)]} \cos 2\theta . \tag{22}$$

This is general for any quadrupole expansion of a circular potential ϕ_0.

Applying equations (21) and (22) to an elliptical power-law surface density, we recover Miralda-Escudé's (1993a) result that for mass profiles steeper than isothermal, the arcs trace ellipses oriented in the same way as the density, whereas for mass profiles less steep than isothermal, these ellipses are oriented perpendicularly to the density.

For the elliptical generalization of the QDEV lens described by equations (1)–(4), the radius of curvature of an arc is given by

$$\left(\frac{R}{r}\right)^{-1} = 1 + 2\epsilon\xi^{-1}\left[\frac{3}{2}\xi^{-1}(1 + \xi^{-1})^3 + 2(1 + \xi^{-1})^3 - 9\xi^{-1}(1 + \xi^{-1})^3 \ln(1 + \xi)\right.$$
$$\left. + 9\xi^{-1}(1 + \xi^{-1})^2 + 3\xi^{-1}(1 + \xi^{-1})(1 + 0.5\xi^{-2}) + \xi^{-3}\right] \cos 2\theta , \tag{23}$$

where we define $\xi = r/r_c$ for notational convenience. Since the QDEV model has finite mass, one expects that far from the lens center, the lens should behave like a circularly symmetric potential, and indeed far from the center where $\xi \gg 1$, $R/r \approx 1$. Note also that $\xi \to \infty$ for the singular model ($r_c = 0$).

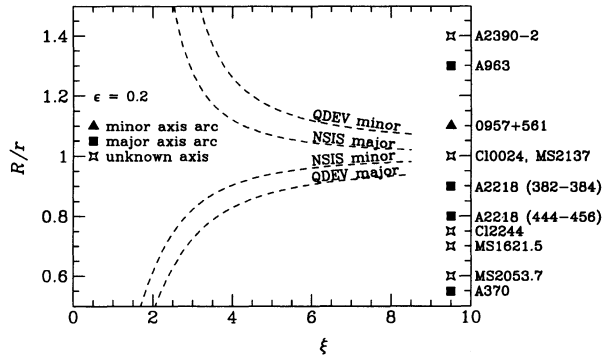

FIG. 10.—The radius of curvature of arcs in NSIS and QDEV lenses as a function of the scaled radius $\xi = r/r_c$. Arcs in a QDEV lens are oriented along ellipses oriented in the same way as the potential. In the NSIS lens, arcs are oriented along a perpendicular ellipse. Curves for the major and minor axes ($\epsilon = 0.2$) are shown separately. Only radii of curvature within $0.5 < R/r < 1.5$ are shown. Outside this range, the quadrupole term of the potential becomes comparable to the monopole, and eq. (22) is invalid. The measured radii of curvature of several giant arcs are shown on the diagram at right. The radii of curvature are consistent with the QDEV model in four of the five cases where the orientation of the lens is apparent to visual inspection, the exception being in A963.

For the elliptical generalization of the NSIS model described by equations (6)–(8), the radius of curvature is given by

$$\left(\frac{R}{r}\right)^{-1} = 1 + 2\epsilon \frac{(1 - 2\xi^{-2})(1 + \xi^{-2}) - 1}{1 + 2\xi^{-2} - 2\xi^{-1}(1 + \xi^{-2})^{1/2}} \cos 2\theta \,. \tag{24}$$

As with the singular QDEV model (a point mass), the singular NSIS model (SIS) has $\xi \to \infty$ and $R/r = 1$, for any ellipticity, as originally noted by Miralda-Escudé (1993a).

The curves described by equations (23) and (24) are plotted in Figure 10 for an ellipticity of $\epsilon = 0.2$ for both the major ($\cos 2\theta = 1$) and minor ($\cos 2\theta = -1$) axes. For the QDEV lens, arcs have $R/r < 1$ on the major axis and $R/r > 1$ on the minor axis, as required for a mass profile steeper than isothermal. For the NSIS lens, the reverse holds.

The radius of curvature R of several giant arcs and arc systems (which appear to trace the arc ellipse) have been listed in Table 2. The values were taken from the literature in the few cases where the numbers were published. In other cases we measured the values off the published pictures. These latter values are probably accurate only to $\pm 10\%$. Also in Table 2 is the distance to the cluster centers r. In some cases the center of the cluster is clearly defined by a dominant central galaxy, but in others it is less obvious. In the case of Cl 2244−02 we took the center in the middle of the group of galaxies bounded by the arc, and in A370 we took the center between the two dominant cD galaxies. The ratio of R/r is listed, and in some cases (especially when $r \lesssim 20''$), it is likely to be uncertain by up to $\pm 30\%$. Where it is possible to determine whether an arc is on the major or minor axis of the lens by visual inspection, an entry is made in the table to indicate which is the case. Our measurements are generally in good agreement with those by Miralda-Escudé (1993a), except for Cl 2244−02 and A370 for which he adopts different cluster centers.

The values of R/r listed in Table 2 are plotted in Figure 10. Among the four arcs which are clearly on the major axis of the lens, three have $R/r < 1$, and the one arc on a minor axis has $R/r > 1$. These observations are consistent with lenses that are steeper than isothermal. The large arc in A963 does not fit this pattern, and the lens must be significantly shallower than isothermal (cf. Miralda-Escudé 1993a). This may be explained by the proximity of this arc to the core of the central cD galaxy.

Additionally, since large arcs are expected to be found on the major axis of elliptical lenses more frequently than on the minor axis (e.g., Grossman & Narayan 1989), the larger number of arcs with $R/r < 1$ compared to the number with $R/r > 1$ also favors lens models that are steeper than isothermal. These arguments favor the QDEV lens model over the NSIS lens model. However, in view of the difficulty in measuring the ratio R/r, these results should be taken merely as suggestive. Images of giant arcs taken in superior seeing obviously will be required for this radius of curvature analysis to be useful.

TABLE 2

OBSERVED RADII OF CURVATURE

Cluster	R	r	R/r	Major/Minor	References
MS 2053.7	10″	17″	0.6	?	1
MS 1621.5	8	12	0.7	?	1
A370	15	30	0.5	major	2
Cl 2244	11	14	0.8	?	2
A2218(444−456)	33	40	0.8	major	3
A2218(382−384)	32	37	0.9	major	3
Cl 0024	35	35	1.0	?	4
MS 2137	16	16	1.0	?	5
0957+561	25	22	1.1	minor	6
A963	24	18	1.3	major	7
A2390−2	14	10	1.4	?	8, 9

REFERENCES.—(1) Lupino & Gioia 1992; (2) Lynds & Petrosian 1989; (3) Pello et al. 1992; (4) Kassiola et al. 1992; (5) Fort et al. 1992; (6) Bernstein et al. 1993; (7) Lavery & Henry 1988; (8) Pello et al. 1991; (9) Fort 1992.

7. CONCLUSION

We have discussed two models for cluster lenses: the nonsingular isothermal sphere (NSIS) and a new model we call quasi–de Vaucouleurs (QDEV). The NSIS lens has been used frequently, and it has the property that for finite core radii, the mass profile is shallower than isothermal, but approaches the isothermal slope asymptotically. The QDEV lens has a surface density profile that resembles that of elliptical galaxies or simulated cluster halos. It is simple in two-dimensional projection, and it has the property that it is steeper than isothermal outside the core, with an asymptotic slope of -3.

For these two models we derived the lensing cross sections for tangential magnification M_T and wrote expressions for the radial magnification M_R. These new results permit the analytical investigation of the statistics of arc lengths and widths. By convolving the cross sections with a simple, but plausible, distribution of source diameters, we compute the statistical distribution of lengths meeting the observational selection criteria of $L/W > 3$ and $L > 2\farcs0$. The latter restriction allows us to account for the effects of finite seeing, since shorter arcs with a minimum width of at least $0\farcs7$ could not meet the L/W restriction too. We emphasize that these simple models do not describe the most accurate predictions for the distributions of arc magnification or arc length, such as found from detailed simulations (Miralda-Escudé 1993a, b; Bergmann & Petrosian 1993), but the differences are small, except in the regime of giant arcs, and we feel our simple models are adequate, given the quality of the data.

Although it is well known that more compact lenses generate more arcs (e.g., Wu & Hammer 1993), arc numbers also depend on the source density and the mass of the lens. To compare data to the lens models, we chose to normalize the length distributions to unity, thereby eliminating the dependence on source density and lens mass, and to make comparisons based on the shapes of the curves. This permits us to add together the data from many clusters, even if they have very different masses or have been surveyed for arcs to different magnitude limits. (This presumes that the arc surveys are not strongly biased against finding arcs at any length, so long as they satisfy the selection criteria. The giant arcs, however, are overrepresented with respect to our simple lens models. This is probably partly physical [Bergmann & Petrosian 1993] and partly selection bias. Giant arcs are still only a small fraction of the total number, and so this bias is of minor significance for our analysis. We note that combining arc data in this way is not legitimate for large arc lengths where the analytic predictions break down.) Thus, our results apply to a characteristic cluster lens and may not be representative of less massive clusters.

We also compare the fraction of arcs that have $W \geq 1\farcs3$ to the predicted fraction, after accounting for selection effects. The strongest constraints on cluster lenses come from this analysis, which essentially is constraining the slope of the lens profile at the radii of the arcs. Adjusting the core radii, which more appropriately should be interpreted as scale or effective radii of the mass profiles, allows us to tune the slope at the arc positions. We conclude that clusters must be at least as compact as $r_c/b \lesssim 0.1$ in the NSIS model. If the QDEV model applies, then $0.5 \lesssim r_c/b \lesssim 0.6$. These numbers assume a slope of the source angular size distribution of $\alpha = 1$, but using a larger value of $\alpha = 2$ increases the upper bounds only a little. The point lens is excluded by both length and width statistics. This is particularly interesting in view of the model of MS 2137 (Mellier, Fort, & Knieb 1993), which is the first clear example of a cluster with a radial arc, implying that the cluster must have a finite core radius. We also note that Petrosian & Lynds (1992) argue that A2218 has a core radius of order the Einstein radius, much larger than our upper limits, but their analysis is based on one weakly distorted arc and assumes a circular source and circular lens, which may be inappropriate for detailed modeling since this cluster shows significant substructure.

If a typical cluster lens has redshift $z = 0.3$, then $b = 20''$ corresponds to $55/h_{100}$ kpc at the lens (assuming $\Omega_0 = 1$, FRW cosmology), so that $r_c \lesssim 5.5/h_{100}$ kpc from the NSIS limit or $r_c \lesssim 33$ kpc from the QDEV limit. Both these constraints are unprecedently small upper limits on cluster core radii. These numbers should be interpreted only as generic values for cluster lenses and should not be presumed to have too much precision, since they are derived from adopting generic cluster parameters.

We derived a general formula for the radius of curvature of arcs in elliptical lenses. We showed that for mass profiles steeper than isothermal, arcs trace ellipses oriented in the same way as the density, but trace ellipses perpendicular to the density for shallower mass profiles. This result was applied to the NSIS and QDEV models. Comparisons of these predictions with the observed radii of curvature of several giant arcs offers some additional evidence in favor of lens models that are steeper than isothermal.

In summary, we conclude that the data, considered in total, show some preference for models such as the QDEV that are steeper than isothermal. Indeed, we strongly confirm Hammer's (1991) conclusion that if most faint field galaxies have diameters of $1''$ or more, then cluster lenses must be steeper than isothermal. We feel, however, that the data do not rule out the NSIS model yet.

The quality of constraints upon lens profiles can best be improved by better observations of arc widths, possibly of sufficient quality to construct a width distribution. To make the fullest use of such data, one will also require improved knowledge about the distribution of unlensed source sizes. Presently, observations show only that a significant fraction of high-redshift sources are marginally resolved, but the actual distribution would be useful. Improved resolution of arc and field galaxy surveys, say with $\sim 0\farcs5$ seeing, may be sufficient to disentangle the effects of the source diameter distribution from the arc width distribution and allow much tighter constraints on the cluster lens mass profile.

It is a pleasure to acknowledge many interesting discussions with N. Kaiser. M. H. Lee is thanked particularly for discussing points of lensing formalism with us and for comments on the manuscript. S. G. acknowledges useful discussions with A. Babul, C. Kochanek, F. Hammer, and R. Narayan, and H.-W. Rix, whom he thanks. This work was supported by NSERC.

APPENDIX A

THE LENGTH DISTRIBUTION OF ARCS

The differential number of arcs at each length L is given by the convolution of the distribution of unlensed angular source size (eq. [18]) with the differential cross section according to

$$\frac{dN}{dL} = \begin{cases} 0, & L < M_T^{\min} L_0^{\min}, \\ \int_{L_0^{\min}}^{L/M_T^{\min}} \frac{d^2N}{d\Omega\, dL_0} \frac{d\sigma}{dM_T} \frac{dL_0}{L_0}, & M_T^{\min} L_0^{\min} < L < M_T^{\min} L_0^{\max}, \\ \int_{L_0^{\min}}^{L_0^{\max}} \frac{d^2N}{d\Omega\, dL_0} \frac{d\sigma}{dM_T} \frac{dL_0}{L_0}, & M_T^{\min} L_0^{\max} < L. \end{cases} \tag{A1}$$

The parameter $M_T^{\min}$ is the value of M_T corresponding to $L/W = 3$. This parameter allows us to count as arcs only images which are more elongated than this. Note that this formula counts only the primary, positive parity arcs outside the Einstein radius of a circular lens. In general, counter arcs can also contribute to this distribution, leading to a discontinuous jump in the differential cross section at some critical magnification (Bergmann & Petrosian 1993). Below this critical magnification, equation (A1) is correct, and above it equation (A1) is accurate to better than a factor of 2. We note, however, that for central densities more than 2.5 times the critical density in the QDEV model, this jump magnification is below 3, and it is always less than 2 in the NSIS model. Thus, the shapes of the curves described by equations (A1) are approximately correct, except at extreme magnifications, where finite source size leads to an excess of giant arcs and then a drop off to zero, since arcs cannot be longer than the circumference of an Einstein ring (Bergmann & Petrosian 1993).

For the particular choice of angular size distribution given by equation (18) with $\alpha = 1$, the indefinite integrals of equation (A1) are

$$\int \frac{d^2N}{d\Omega\, dL_0} \frac{d\sigma}{dM_T} \frac{dL_0}{L_0} = \pi b^2 C \left[\frac{1}{L - L_0} + \frac{L - L_0}{L^2} - 2 \frac{r_c}{b} \frac{L_0^2}{L^{5/2}(L - L_0)^{1/2}} + \left(\frac{r_c}{b}\right)^2 \frac{L_0^2}{L^3} \right] \tag{A2}$$

for the QDEV lens, and

$$\int \frac{d^2N}{d\Omega\, dL_0} \frac{d\sigma}{dM_T} \frac{dL_0}{L_0} = \pi b^2 C \left[\frac{L_0}{(L - L_0)^2} - \frac{1}{L - L_0} - 2 \frac{r_c}{b} \left(\frac{L - L_0}{L^2} + \frac{1}{L - L_0} \right) \right] \tag{A3}$$

for the NSIS lens. To obtain the differential length distribution, we merely evaluate these functions at the upper and lower bounds of integration. The cumulative distributions $N(>L)$ can also be derived analytically in both cases, but the results are lengthy, and we do not reproduce them here.

APPENDIX B

THE RADIUS OF CURVATURE OF AN ARC IN A GENERAL POTENTIAL

The principal axes of the magnification matrix M (or of M^{-1}) define the local orientation of arc length and widths. The change of orientation of the principal axes along the length of an arc defines its radius of curvature.

We begin the derivation of the radius of curvature of an arc by giving a simple derivation of M^{-1} in polar form. Consider the tensor

$$\nabla\nabla\tilde{\phi} = \left(\hat{e}_r \frac{\partial}{\partial r} + \frac{\hat{e}_\theta}{r} \frac{\partial}{\partial \theta} \right) \left(\hat{e}_r \frac{\partial}{\partial r} + \frac{\hat{e}_\theta}{r} \frac{\partial}{\partial \theta} \right) \tilde{\phi}, \tag{B1}$$

where $\tilde{\phi}$ is the dimensionless reduced potential, related to ϕ by

$$\tilde{\phi} = \frac{2}{c^2} \frac{D_{LS}}{D_{OL} D_{OS}} \phi. \tag{B2}$$

Noting that the derivatives of the unit vectors are

$$\frac{\partial}{\partial r} (\hat{e}_r, \hat{e}_\theta) = (0, 0); \qquad \frac{\partial}{\partial \theta} (\hat{e}_r, \hat{e}_\theta) = (\hat{e}_\theta, -\hat{e}_r), \tag{B3}$$

we can expand equation (B1) into

$$\nabla\nabla\tilde{\phi} = (\hat{e}_r \quad \hat{e}_\theta) \begin{bmatrix} \frac{\partial^2 \tilde{\phi}}{\partial r^2} & \frac{\partial}{\partial r} \left(\frac{1}{r} \frac{\partial \tilde{\phi}}{\partial \theta} \right) \\ \frac{\partial}{\partial r} \left(\frac{1}{r} \frac{\partial \tilde{\phi}}{\partial \theta} \right) & \frac{1}{r} \frac{\partial \tilde{\phi}}{\partial r} + \frac{1}{r^2} \frac{\partial^2 \tilde{\phi}}{\partial \theta^2} \end{bmatrix} \begin{pmatrix} \hat{e}_r \\ \hat{e}_\theta \end{pmatrix}. \tag{B4}$$

The components of M^{-1} are simply the components of $1-\nabla\nabla\tilde{\phi}$, and in polar coordinates we write

$$M^{-1}=\begin{pmatrix}1-\kappa-\lambda & -\mu\\ -\mu & 1-\kappa+\lambda\end{pmatrix}, \tag{B5}$$

where

$$\kappa=\frac{1}{2}\left(\frac{\partial^2\tilde{\phi}}{\partial r^2}+\frac{1}{r}\frac{\partial\tilde{\phi}}{\partial r}+\frac{1}{r^2}\frac{\partial^2\tilde{\phi}}{\partial\theta^2}\right),\qquad \lambda=\frac{1}{2}\left(\frac{\partial^2\tilde{\phi}}{\partial r^2}-\frac{1}{r}\frac{\partial\tilde{\phi}}{\partial r}-\frac{1}{r^2}\frac{\partial^2\tilde{\phi}}{\partial\theta^2}\right),\qquad \mu=\frac{\partial}{\partial r}\left(\frac{1}{r}\frac{\partial\tilde{\phi}}{\partial\theta}\right). \tag{B6}$$

The orientation ϑ of the principal axes of an arc is defined by the rotation β that diagonalizes the matrix M^{-1} and by the azimuthal position θ where the measurement is made. Then the angular orientation of an arc with respect to a Cartesian coordinate system is given by

$$\vartheta=\theta+\beta\,, \tag{B7}$$

where the angle β by which the $(\hat{e}_r, \hat{e}_\theta)$ basis must be rotated to diagonalize M^{-1} is given by

$$\beta=\tan^{-1}\left(\frac{\mu}{\lambda}\right). \tag{B8}$$

The radius of curvature of the arc is given by

$$R=\frac{ds}{d\vartheta}\,, \tag{B9}$$

where ds is the differential length along the arc,

$$ds=d\theta\sqrt{r^2+\left(\frac{dr}{d\theta}\right)^2}\,. \tag{B10}$$

From equation (B7), one obtains

$$d\vartheta=d\theta\left(1+\frac{d\beta}{d\theta}\right)=d\theta\left(1+\frac{\partial\beta}{\partial\theta}+\frac{\partial\beta}{\partial r}\frac{dr}{d\theta}\right). \tag{B11}$$

The total derivative $dr/d\theta$ is to be taken along the arc, and from the geometry we see that

$$\frac{dr}{d\theta}=-r\tan\beta\,. \tag{B12}$$

Substituting equations (B10)–(B12) into (B9) and simplifying, we obtain

$$\left(\frac{R}{r}\right)^{-1}=\left(1+\frac{\partial\beta}{\partial\theta}-r\tan\beta\,\frac{\partial\beta}{\partial r}\right)\cos\beta\,. \tag{B13}$$

If the cross term μ of the magnification matrix is small, then β and $d\lambda/d\theta$ are $O(\mu)$ since β, $d\lambda/d\theta$, and μ are all of order ϵ. Then, substituting equation (B8) into equation (B13), we get

$$\left(\frac{R}{r}\right)^{-1}=1+\frac{1}{2\lambda}\frac{\partial\mu}{\partial\theta}+O(\mu^2)\,. \tag{B14}$$

This is completely general for any potential $\tilde{\phi}$.

REFERENCES

Bahcall, N. A., & Cen, R. 1993, ApJ, 407, L49
Bergmann, A. G., & Petrosian, V. 1993, ApJ, 413, 18
Bergmann, A. G., Petrosian, V., & Lynds, R. 1990, ApJ, 350, 23
Bernstein, G. M., Tyson, J. A., & Kochanek, C. S. 1993, AJ, 105, 816
Binney, J. 1982, MNRAS, 200, 951
Binney, J., & Tremaine, S. 1987, Galactic Dynamics (Princeton Univ. Press)
Blandford, R. D., & Kochanek, C. S. 1987, ApJ, 321, 658
Blandford, R. D., & Narayan, R. 1986, ApJ, 310, 568
———. 1992, ARA&A, 30, 311
Ellis, R., Allington-Smith, J., & Smail, I. 1991, MNRAS, 249, 184
Dubinski, J., & Carlberg, R. G. 1991, ApJ, 378, 496
Dyer, C. C. 1984, ApJ, 287, 26
Ellis, R., Allington-Smith, J., & Smail, I. 1991, MNRAS, 249, 184
Fort, B. 1992, in Gravitational Lenses, ed. R. Kayser, T. Schramm, & L. Nieser (Berlin: Springer), 267
Fort, B., Le Fevre, O., Hammer, F., & Cailloux, M. 1992, ApJ, 399, L125
Fort, B., Prieur, J. L., Mathez, G., Mellier, Y., & Soucail, G. 1988, A&A, 200, L17
Giraldi, M., Biviano, A., Giuricin, G. Mardirossian, F., & Mezzetti, M. 1993, ApJ, 404, 38
Giraud, E. 1988, ApJ, 334, L69
Grossman, S. A. 1994, in Gravitational Lenses in the Universe, ed. J. Surdej et al. (Université de Liège), in press
Grossman, S. A., & Narayan, R. 1988, ApJ, 324, L37
———. 1989, ApJ, 344, 637
Hammer, F. 1991, ApJ, 383, 66
Hammer, F., & Rigaut, F. 1989, A&A, 226, 45
Hammer, F., Le Fevre, O., Jones, J., Rigaut, F., & Soucail, G. 1989, A&A, 208, L7
Hernquist, L. 1990, ApJ, 356, 359
Hinshaw, G., & Krauss, L. M. 1987, ApJ, 320, 468
Jaffe, W. 1983, MNRAS, 202, 995
Kaiser, N., & Squires, G. 1993, ApJ, 404, 441
Kassiola, A., Kovner, I., & Fort, B. 1992, ApJ, 400, 41
Kneib, J.-P., Mellier, Y., Fort, B., & Mathez, G. 1993, A&A, 273, 367
Kochanek, C. S. 1990, MNRAS, 274, 135

Kochanek, C. S. 1991, ApJ, 373, 354
Kovner, I. 1987, ApJ, 312, 22
Lavery, R. J., & Henry, J. P. 1988, ApJ, 329, L21
Lilly, S. J., Cowie, L. L., & Gardner, J. P. 1991, ApJ, 369, 79
Luppino, G. A., & Gioia, I. M. 1992, A&A, 265, L9
Lynds, R., & Petrosian, V. 1986, Bull. AAS, 18, 1014
———. 1989, ApJ, 336, 1
Maoz, D., & Rix, H.-W. 1993, ApJ, in press
Mathez, G., Fort, B., Mellier, Y., Picat, J.-P., & Soucail, G. 1992, A&A, 256, 343
Mellier, Y., Fort, B., & Knieb, J.-P. 1993, ApJ, 407, 33
Mellier, Y., Fort, B., Soucail, G., Mathez, G., & Cailloux, M. 1991, ApJ, 380, 334
Miller, J. S., & Goodrich, R. W. 1988, Nature, 331, 685
Miralda-Escudé, J. 1991, ApJ, 370, 1
———. 1993a, ApJ, 403, 497
———. 1993b, ApJ, 403, 509
Nemiroff, R., & Dekel, A. 1989, ApJ, 344, 51
Pello, R., Le Borgne, J. F., Sanahuja, B., Mathez, G., & Fort, B. 1992, A&A, 266, 6
Pello, R., Le Borgne, J. F., Soucail, G., Mellier, Y., & Sanahuja, B. 1991, ApJ, 366, 405
Pello-Descayre, R., Soucail, G., Sanahuja, B., Mathez, G., & Ojero, E. 1988, A&A, 190, L11
Petrosian, V., & Lynds, R. 1992, in Gravitational Lenses, ed. R. Kayser, T. Schramm, & L. Nieser (Berlin: Springer), 305
Press, W. H., Flannery, B. P., Teukolsky, S. A., & Vetterling, W. T. 1986, Numerical Recipes (Cambridge Univ. Press)
Sanitt, N. 1976, MNRAS, 174, 91
Schneider, P., & Weiss, A. 1991, A&A, 247, 269
Smail, I., Ellis, R. S., Fitchett, M. J., Nørgaard-Nielsen, H. U., Hansen, L., & Jørgensen, H. E. 1991, MNRAS, 252, 19
Soucail, G., Fort, B., Mellier, Y., & Picat, J. P. 1987a, A&A, 172, L14
Soucail, G., Mellier, Y., Fort, B., Hammer, F., & Mathez, G. 1987b, A&A, 184, L7
Soucail, G., Mellier, Y., Fort, B., Mathez, G., & Cailloux, M. 1988, A&A, 191, L19
Turner, E. L., Ostriker, J. P., & Gott, J. R. 1984, ApJ, 284, 1
Tyson, J. A. 1988, AJ, 96, 1
Tyson, J. A., Valdes, F., & Wenk, R. 1990, ApJ, 349, L1
Wallington, S., & Narayan, R. 1993, ApJ, 403, 517
Wambsganss, J., Giraud, E., Schneider, P., & Weiss, A. 1989, ApJ, 337, L73
Wu, X. P. 1989, A&A, 214, 43
———. 1993, ApJ, 411, 513
Wu, X. P., & Hammer, F. 1993, MNRAS, 262, 187